IEEE Access
Multidisciplinary | Rapid Review | Open Access Journal

Received March 12, 2022, accepted April 11, 2022, date of publication April 18, 2022, date of current version April 29, 2022.

Digital Object Identifier 10.1109/ACCESS.2022.3168666

Dynamics and Energy Analysis of Nonequatorial Space Elevator Using Three-Dimensional Nonlinear Finite Element Method Extended to Noninertial Coordinate System

RYO KUZUNO, SHUONAN DONG, TAIKI OKADA, KEISUKE OTSUKA, AND KANJURO MAKIHARA

Department of Aerospace Engineering, Tohoku University, Sendai, Miyagi 980-8579, Japan

Corresponding authors: Ryo Kuzuno (ryo.kuzuno.q1@dc.tohoku.ac.jp) and Kanjuro Makihara (kanjuro.makihara.e3@tohoku.ac.jp)

This work was supported by the Japan Society for the Promotion of Science (JSPS) Grants-in-Aid for Scientific Research under Grant 20K22378, Grant 21K14341, and Grant 20K21041.

ABSTRACT A space elevator is a futuristic space transportation technology that enables low-cost and versatile payload transportation using climbers on a tether deployed from the geostationary orbit (GEO). In particular, a nonequatorial space elevator, which contains an anchor in a region with latitudes on the Earth, has recently attracted attention. It has several advantages, such as extending the construction range and avoiding collisions with spacecraft in the GEO. Prior research has focused on rigid-body or spring-mass models with low fidelity. This paper proposes a modeling method for nonequatorial space elevators using a nodal-position finite element method (NPFEM) extended to a rotational coordinate system. The NPFEM is a three-dimensional finite element method that considers geometric nonlinearity. Conventional NPFEMs have only been formulated using inertial coordinate systems. This paper proposes a method to formulate the NPFEM in a noninertial coordinate system and derive the inertial forces and Jacobian matrices. In addition, a three-dimensional analysis of a nonequatorial space elevator was performed based on the proposed method. After determining the equilibrium position of the NPFEM, the dynamic response of the tether during climber ascent was analyzed. Moreover, parametric studies were conducted by varying several properties of the nonequatorial space elevator. Furthermore, the energy exchange between the components was analyzed to validate the proposed method and to discuss the energy perspective of the space elevator. The results revealed that the proposed nonequatorial space elevator model experienced a more tensioned equilibrium and exhibited a more significant dynamic response than conventional models.

INDEX TERMS Space elevator, nonequatorial, NPFEM, dynamic response, energy exchange.

NOMENCLATURE

A	Cross-sectional area of tether.
A_a	Cross-sectional area of tether at anchor point.
E	Modulus of longitudinal elasticity.
K	Kinetic energy.
l	Length of tether element after deformation.
l_0	Length of tether element before deformation.
m_{cl}	Mass of climber.
m_{cw}	Mass of counterweight.
$\mathbf{M}$	Mass matrix.
N_{ele}	Number of elements.
N_{rate}	Ratio of period for acceleration/deceleration to overall ascent period.
$\mathbf{q}$	Generalized coordinate vector.
$\mathbf{Q}_{el}$	Generalized elastic force vector.
$\mathbf{Q}_g$	Generalized gravitational force vector.
$\mathbf{Q}_c$	Generalized centrifugal force vector.
$\mathbf{Q}_{Co}$	Generalized Coriolis force vector.
$\mathbf{r}$	Position vector.
$\mathbf{S}$	Shape function.
T_{climb}	Total ascending period for climber.
U_{el}	Elastic potential energy.
U_g	Potential energy due to gravitational force.
U_c	Potential energy due to centrifugal force.
v_{rmax}	Maximum relative velocity of climber to tether.

The associate editor coordinating the review of this manuscript and approving it for publication was Rosario Pecora.

x_{cl}	Position of climber in local coordinate system.
μ	Geocentric constant
ρ	Material density of tether.
σ_{a}	Allowable stress of tether.
ω_{E}	Angular velocity of rotation of the Earth.
$\boldsymbol{\Omega}_{\mathrm{E}}$	Angular velocity vector of rotation of the Earth.
θ_{a}	Anchor latitude.
φ_{a}	Anchor longitude.
γ	Second-order time derivative of constraint equation for climber.
$()_{\mathrm{cw}}$	Vector or matrix for counterweight.
$()_{\mathrm{cl}}$	Vector or matrix for climber.
$()_{\mathrm{t}}$	Vector or matrix for one tether element.
$()_{\mathrm{t\text{-}all}}$	Superposed vector or matrix composed of all tether elements.
$()_{\mathrm{entire}}$	Vector or matrix for entire space elevator system.

I. INTRODUCTION

A. STUDY BACKGROUND

1) SPACE ELEVATOR

The space elevator concept holds enormous potential for futuristic space transportation, as it can transport payloads on a climber that moves on a tether deployed from a geostationary orbit (GEO) toward the Earth and deep space. Artsutanov [1] pioneered the idea of space elevators, and subsequently, Pearson [2] submitted a technical paper that triggered scientific research regarding this innovative concept. Although the limitation of suitable materials remains a bottleneck, the discovery of carbon nanotubes (CNTs) by Iijima [3] convinced NASA [4] and Edwards [5] to seriously consider their feasibility in constructing a space elevator. Space elevators are expected to be a futuristic means of space transportation and traffic owing to their low cost and reusability. Nonetheless, there are still several issues regarding space elevators, such as the strength of tether materials, manufacturing technology for long tethers, and tether rupture caused by space debris. In general, numerical simulations are employed to comprehend the tether dynamics of space elevators. Pearson [2] modeled a tether as a string considering its high tension and low bending stiffness and analyzed their modal oscillations. Pearson [2] also proposed a tapered cross-section to maintain constant stress across the tether, regardless of the location, for safety purposes. Subsequently, Cohen and Misra [6] proposed a tapered model considering the elongation and deformation of the tether under its own weight. In addition to analyzing the modal oscillations of the tether, Cohen and Misra [7] evaluated the tether deformation based on the mass of the climber. They clarified that considering the climber mass influences the tether oscillation.

2) NONEQUATORIAL SPACE ELEVATOR

Most space elevators discussed to date are based on a simple concept: the tether connects to the equatorial plane of the Earth. In 2004, Gassend [8] proposed a model in which the tether was connected to a nonequatorial plane of the Earth. In particular, the nonequatorial space elevator offers the following advantages: 1) expansion of the possible construction area, 2) avoidance of collision with spacecraft in the GEO, 3) avoidance of high-radiation area of cosmic rays (Van Allen belt), and 4) avoidance of collision with Phobos and Deimos (for Mars elevator). Advantage 1 can contribute to expanding the technical options to consider the anchor location from a geopolitical perspective, and advantage 2 is essential for the environmental protection of GEO and benefits the system sustainability of space elevators. Regarding advantage 3, the Van Allen belt—a strong radiation belt containing protons and electrons captured by the Earth's magnetic field—surrounds the Earth in a toroidal shape. Space elevators are expected to travel through space more slowly than rockets. Therefore, diminishing the influence of the Van Allen belt is of considerable advantage in the case of crewed space transportation using space elevators. Because the thickness of the Van Allen belt is highest near the equator, the placement of the anchor at a higher latitude mitigates the influence of the Van Allen belt [9]. Advantage 4 would aid the construction of space elevators on Mars. This advantage led to the proposal of nonequatorial space elevators for the Mars migration program [10]. Although nonequatorial space elevators possess these attractive possibilities, the direction of the forces acting on the tether is more complicated than that of equatorial space elevators, which creates challenges during the analysis.

3) ANALYSIS OF TETHER DYNAMICS IN SPACE

The tether dynamics in space has been analyzed for various situations. Takeichi [11] and Tao *et al.* [12] analyzed the behavior of tether deployment during construction. Aslanov *et al.* [13] proposed a simulation method for the tether rupture behavior. In particular, the tether motion during climber ascent should be analyzed to validate the system feasibility and design the maximum payload and operating speed of space elevators. The tether dynamics analysis at climber ascent was first modeled by McInnes [14] in 2005 as a particle moving on a tether. Subsequently, Cohen and Misra [15] modeled the climber as a lumped mass and the tether as rigid bars. The results revealed that the tether oscillated in the equatorial plane because of the Coriolis force excited by a moving climber. Accordingly, Williams and Ockels [16] and Ishikawa *et al.* [17] proposed methods for suppressing these oscillations. The dynamics of partial space elevators, wherein the tether is not connected to the Earth, have also been actively studied. Williams [18] proposed a spring-mass model with multiple degrees of freedom for the dynamics of a climber ascending and descending on a tether of a partial space elevator. Shi *et al.* [19] proposed an optimal operation method and analyzed the tether oscillations of multiple climbers on a partial space elevator. Future research should clarify the effects of external disturbances such as the oblateness of the Earth, atmosphere, heat, and perturbations by the Moon and Sun.

4) ANALYSIS OF TETHER DYNAMICS IN NONEQUATORIAL SPACE ELEVATOR

To date, several studies have been conducted on the statics and dynamics of nonequatorial space elevators. Gassend [8] studied the latitudinal range applicable for nonequatorial space elevators. Subsequently, Cowan and Leonard [10] modeled the tether as rigid bar elements, and Wang *et al.* [20] proposed a multibody-rigid-bar model and a spring-mass model with multiple degrees of freedom applicable for nonequatorial space elevators and obtained the equilibrium position. Moreover, Wang *et al.* [21] analyzed the oscillation modes of the tether of a nonequatorial space elevator using a spring-mass model with multiple degrees of freedom. They also analyzed tether dynamics during climber ascent. Their research clarified the dynamic response of a nonequatorial space elevator during climber ascent. Prior studies have clarified the fundamental tether dynamics of space elevators during climber ascent. However, only certain high-fidelity models accurately represent the deformation of flexible structures such as tethers. For instance, the model developed by Wang *et al.* [21] exhibited low fidelity because they neglected the continuity in the elements and the geometric nonlinearity of the tether. Thus, a model that can analyze the deformation of tethers with high fidelity is essential to study the feasibility of space elevators in detail.

In general, the finite element method (FEM) is used as an analysis method to consider the deformation of a structure. The FEM enables the analysis of beams with complex shapes such as stepped beams. However, the conventional linear FEM is unsuitable for flexible structures such as tethers because it cannot accurately represent large deformations in systems that include rigid body motion components. Recently, nonlinear FEMs that can accurately represent large deformations of flexible structures have garnered considerable attention, as reflected by their application in numerous studies. Shabana [22] proposed the absolute nodal coordinate formulation (ANCF), and Zhu *et al.* [23], [24] proposed the nodal-position FEM (NPFEM) in 2003. Consequently, Luo *et al.* [25] modeled an equatorial space elevator using ANCF and conducted a static analysis. Meanwhile, dynamic analysis (i.e., time evolution problems) requires a long computation period for large systems such as space elevators. Therefore, the computational efficiency of nonlinear FEMs should be improved for the application in space elevator analysis. Accordingly, we will apply NPFEM to analyze nonequatorial space elevators by extending to a noninertial frame. In the NPFEM, each element is modeled as straight, considering only the elongational deformation. In addition, its generalized coordinates are positions in the absolute coordinate system. Consequently, the coupling of elastic deformation in the elongation direction and the rigid body rotation of each element can be efficiently described in three dimensions. Moreover, the NPFEM approximates the mass matrix as a constant, which is substantially advantageous for improving the computational efficiency of the dynamic analysis. The NPFEM employs fewer variables than the ANCF [26], even when applying low-order gradient-deficient ANCF elements that are widely used for aerospace structures [27]–[29]. This enables efficient three-dimensional simulation. Moreover, when formulating a long tether with a polynomial approximation function such as ANCF, the equation of motion needs to be nondimensionalized because it can significantly exceed the order of magnitude retained by the computer [30]. In contrast, an NPFEM element does not require nondimensionalization due to its linear shape function. Owing to its desirable advantages, the NPFEM has been considered suitable for analyzing flexible tether, e.g., dynamics analysis of a towing tether for a submarine [31] and a conductive tether for debris removal [32]. Li *et al.* [33] analyzed the impact of ascending and descending multiple climbers on tether dynamics in three dimensions using NPFEM. However, it poses a limitation in the analysis for nonequatorial space elevators. The conventional NPFEM is formulated only in the inertial coordinate system, not the noninertial coordinate system. As the nonequatorial space elevator is subject to complex force directions in three dimensions, the equilibrium position used for the initial position cannot be obtained intuitively, such as for an equatorial space elevator. Thus, the equilibrium position of the space elevator must be determined using a static analysis. When utilizing the NPFEM model to represent geometric nonlinearity, the equilibrium position of the space elevator in the NPFEM model must be known. However, the NPFEM model formulated in the conventional inertial coordinate system cannot conveniently analyze the space elevator because the space elevator rotates at the same angular velocity as the Earth.

B. RESEARCH OBJECTIVE

This paper pursues three objectives. First, we propose a nonequatorial space elevator analysis model with higher fidelity than conventional approaches. Although Wang *et al.* [21] developed simple models such as rigid bars and spring masses to analyze the nonequatorial space elevator, the rigid bar model cannot deal with the deformation in the tether element. In addition, the spring-mass model cannot represent the gravity gradient, and the geometric nonlinearity is neglected in the conventional model proposed by Wang *et al.* [21]. In a large system such as a space elevator, the inclusion or exclusion of these considerations when constructing the model can significantly impact its equilibrium position and dynamics. This paper proposes a nonequatorial space elevator analysis model that extends the NPFEM in order to represent the rigid body motion and the elastic deformation of the tether. Moreover, the coupling effect between the motions of the climber and of the counterweight exists in this model. Generally, nonlinear FEMs are computationally more expensive than spring-mass models due to their multiple degrees of freedom. Although Luo *et al.* [25] utilized the ANCF to analyze the static problem of an equatorial space elevator, the solution of the time-evolution problem for a large-scale system such as the space elevator requires computational efficiency. Since the NPFEM neglects the bending

deformation and the corresponding elastic force, it has fewer degrees of freedom than the ANCF. Therefore, we adopted the NPFEM.

Second, we propose a method to formulate the NPFEM model with geometric nonlinearities in a three-dimensional Cartesian noninertial coordinate system. Due to the three-dimensional gravitational field, the nonequatorial space elevator is subject to a complicated equilibrium position. Hence, a simple equilibrium position such as a straight tether is not provided. Wang *et al.* [21] adopted a three-dimensional Cartesian rotational coordinate system and obtained the equilibrium position using static analysis prior to dynamic analysis. On the other hand, the conventional NPFEM model has been formulated only in the inertial coordinate system. A model formulated in an inertial coordinate system unnecessarily increases the complexity when deriving the equilibrium position of a nonequatorial space elevator. Therefore, this paper proposes an NPFEM model described in a rotational coordinate system. The equilibrium position of the NPFEM model described in the rotational coordinate system should be obtained to realize dynamic analysis. Furthermore, we propose a method to derive the generalized inertial force vectors and their Jacobian matrices. Luo *et al.* [25] described the ANCF in a rotational coordinate system and formulated the centrifugal force. However, in this paper, we formulated the Coriolis force in addition to the centrifugal force. It allowed us to analyze the dynamics more precisely.

Lastly, the energy of a nonequatorial elevator system was analyzed to reveal the energy exchanges occurring between the climber and the tether–counterweight system because the energy flowing into the tether has not been quantitatively discussed in prior space elevator dynamic analyses at climber ascent. This paper discusses the energy exchange between the climber and the tether–counterweight system of a nonequatorial space elevator based on the dynamic analysis results of a nonlinear FEM. The current model considers the coupling effect between the climber and the tether. It is valuable in considering the feasibility of a space elevator from an energy perspective.

The remainder of this paper is organized as follows. The basic model of the analysis is presented in Section II, wherein the basic parameters such as the total tether length, tether material, and anchor latitude are set. After that, these parameters are used to determine the properties of the tapered cross-sectional area and counterweight mass for the nonequatorial space elevators anchored at various latitudes. In Section III, the nonequatorial space elevator components: the tether, counterweight, and climber, are formulated, extending the NPFEM to the noninertial frame. Subsequently, the static and dynamic analyses of the tether are conducted in Section IV, wherein the obtained results were compared with those evaluated using other models. In addition, the results of the parametric studies under various climber mass and climber velocity conditions are discussed in this section. Moreover, the proposed method is verified and discussed based on the energy exchange between components in nonequatorial space elevators. Lastly, the results, findings, future challenges, and future research directions are summarized in Section V.

II. PARAMETER DETERMINATION IN ANALYSIS OF NONEQUATORIAL SPACE ELEVATOR

A. DESCRIPTION OF ANALYSIS MODEL

The coordinate system used in this paper is illustrated in Fig. 1, wherein a three-dimensional Cartesian coordinate system with the center of the Earth at origin O is described. The X–Y plane denotes the equatorial plane, and the Z-axis represents the rotation axis of the Earth. Overall, the coordinate system is a noninertial coordinate system rotating around the Z-axis with an angular velocity ω_{E}, where ω_{E} indicates the angular velocity of the rotation of the Earth. In addition, the X-axis denotes the line connecting the latitude and longitude 0° on the Earth and origin O; the Y-axis is considered a right-handed Cartesian coordinate system. The gravitational and inertial forces act in this rotational coordinate space. Rigorously, the Earth revolves around the Sun. However, this paper neglects inertial effects related to the Earth's orbital revolution. A space elevator comprises a tether, climber, counterweight, and anchor connecting the tether to the Earth. The counterweight helps maintain the mechanical balance of the space elevator even for a short tether; thus, it can help reduce the oscillation amplitude of the tether. It was assumed that both the climber and the counterweight were lumped masses, and the Earth was assumed to be a perfect sphere (zero oblateness). The effects of disturbances such as tidal forces of the Sun and moon, atmospheric loads, solar wind, and temperature variations were neglected. The overall length of the tether was set to 1.0×10^8 m following Edwards' prior study [5].

The tether material was assumed to be composed of carbon nanotubes (CNTs), discovered by Iijima [3] in 1991. To date, several experiments have been conducted to understand the mechanical properties of CNTs. Salvetat *et al.* [34] estimated the elastic modulus of single-walled carbon nanotubes (SWCNTs) as 1.0×10^3 GPa, considered in this study. Walters *et al.* [35] conducted tensile testing of ropes composed of bundled fibers and determined the elastic range of SWCNTs extended up to 5.8%. In this experiment [35], the elastic elongation rate of CNTs was measured by moving the tip of an atomic force microscope perpendicular to the SWCNT rope and translating the force acting on the SWCNT into tension. Yu *et al.* [36] conducted tensile tests on SWCNT ropes and observed approximately 1.1–5.3% elastic strains. In comparison, Takakura *et al.* [37] observed a tensile strength of approximately 6.6×10^2 GPa. As discussed above, several scholars have conducted tests to determine the tensile strength of CNTs. However, most results do not correspond with theoretical ones because producing high-purity CNTs without any defects and recording experimental measurements with these CNTs are challenging. The strength of CNTs is highly dependent on their structure, pressure,

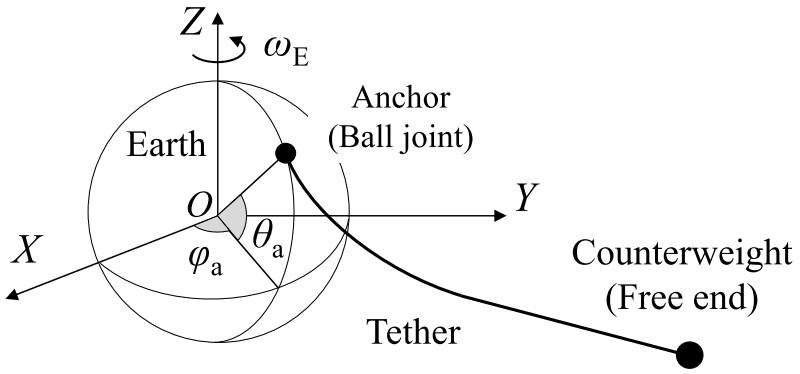

FIGURE 1. Components of space elevator and coordinate system of analysis model.

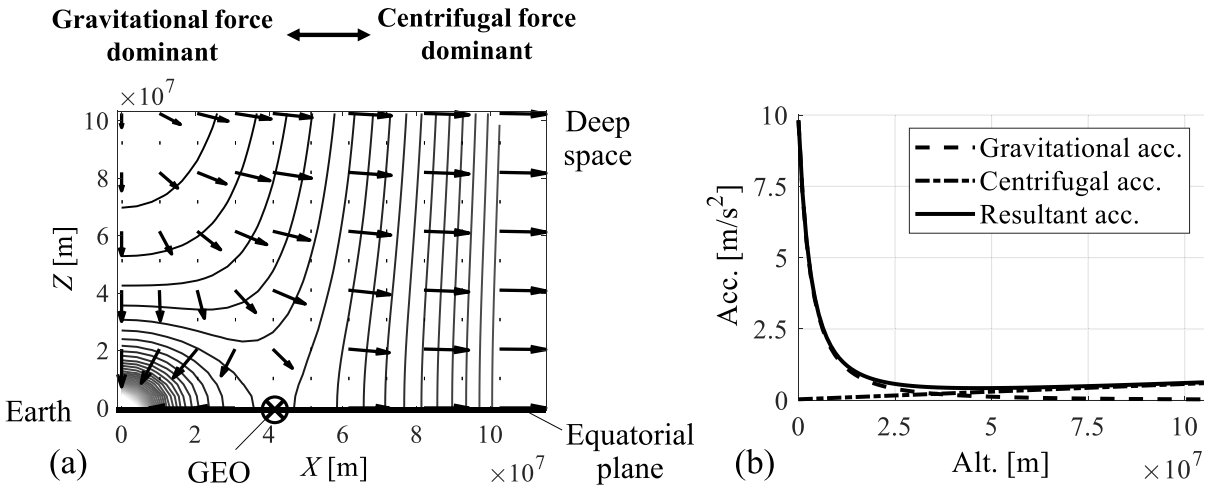

FIGURE 2. (a) Resultant force vector of gravitational and centrifugal forces, (b) gravitational and centrifugal acceleration field of the Earth at each altitude.

temperature, measurement method, synthesis method, and so on. Therefore, this paper assumed an elastic elongation rate of approximately 4% (reference stress: 4.0×10^2 GPa), referring to the experiments of Walters *et al.* [35]. The safety factor was set as 2 [38], and the allowable stress σ_a was assumed to be 2.0×10^2 GPa.

B. TETHER CROSS-SECTIONAL AREA

The magnitude and direction of the gravitational and centrifugal forces acting on an object vary in their spatial positions. A tether with a constant cross-sectional area is undesirable and poses safety concerns because the magnitude of the stress acting on the tether varies with its position. Therefore, a tapered shape with varying cross-sectional areas depending on its position is generally considered. An appropriate setting of the tapered shape avoids strong local stresses and uniformly distributes constant stress. In 1975, Pearson [2] conducted the first study of tapered cross-sectional properties with constant stress at equilibrium. However, Pearson's study did not consider the elongation of the tether under its own weight. After that, Cohen and Misra [6] proposed a tapered shape considering the elongation and deformation of the tether under its own weight.

In nonequatorial space elevators, the direction of the combined gravitational and centrifugal forces is complicated, which creates difficulty in deriving the characteristics of the tapered cross-sectional area using analytical methods. In context, Wang *et al.* [20] proposed a numerical method to determine the tapered shape of a nonequatorial space elevator under constant stress for a rigid bar and spring-mass model. Wang *et al.* [20] formulated the rigid bar model in a two-dimensional planar coordinate system comprising the X–Z axes. As reported, the same gravitational and centrifugal forces can be obtained on any two-dimensional plane containing the rotation axis [8]. Notably, the division into a two-dimensional plane is effective only if no force exists outside the plane, including the rotation axis. In the static case, it can be considered in a two-dimensional plane. The X–Z coordinate system plotted in the two-dimensional plane is presented in Fig. 2, including the Z-axis: the rotation axis. As indicated, the gravitational force was dominant in the region proximate to the Earth than in the GEO radius of

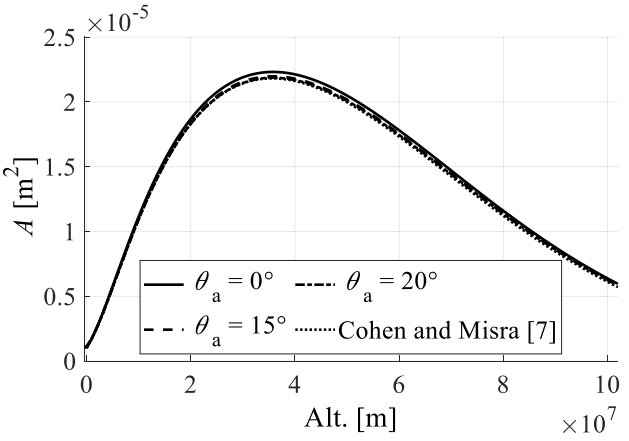

FIGURE 3. Tether cross-sectional area at each altitude for nonequatorial space elevator.

4.1 × 10^7 m. In contrast, the centrifugal force caused by the rotation of the Earth was dominant in the region located farther from the GEO radius. In the rigid bar model proposed by Wang *et al.* [20], the tether is divided into rigid bar elements, and the unknowns represent the cross-sectional area of each node, magnitude and direction of the acting tension, and angle between the rigid bar and equatorial plane. The solution for these unknowns with a solver yields the tapered cross-sectional area characteristics. The problem was solved using the solver function "FSOLVE" in MATLAB. The comparison of the tether cross-sectional area for the varying anchor latitude θ_a is depicted in Fig. 3.

The number of elements N_{ele} was set to 100, and the cross-sectional area of the node connected to the anchor was set as 1.0 × 10^{-6} m^2. The anchor latitude θ_a was varied within 0–20°. The tapered cross-section of the nonequatorial space elevator evaluated using the rigid bar model provided by Wang *et al.* [20] was consistent with the analytically obtained cross-section characteristics of the equatorial space elevator [6]. Notably, the cross-sectional characteristics did not significantly vary with the latitude of the anchor. The counterweight mass values at each latitude are also listed in Table 1, which implies that a counterweight mass of approximately 2.0 × 10^5 kg could achieve the mechanical equilibrium of the system at any anchor latitude. Overall, no solution could be found at latitudes greater than 20°. The results provided by Wang *et al.* [20] revealed the range of the solution was up to approximately 20° anchor latitude for an allowable stress σ_a of 20 GPa on a tether, which is consistent. Furthermore, the cross-sectional area obtained in the rigid bar model was attributed to each nodal point. Therefore, when applying a nonlinear FEM, the cross-sectional area should be converted to an area acting on each element. This paper assumed that the cross-sectional area of each element was constant, and thus, the cross-sectional area in an element $A_{i\text{th-element}}$ was evaluated as the average of the cross-sectional areas $A_{i\text{-node}}$ and $A_{i+1\text{-node}}$ of the nodes at both ends of the element, expressed as

$$A_{i\text{th-element}} \equiv \frac{A_{i\text{-node}} + A_{i+1\text{-node}}}{2}. \tag{1}$$

TABLE 1. Counterweight mass m_{cw} at each anchor latitude θ_a.

Anchor latitude θ_a [deg]	0	15	20
Counterweight mass m_{cw} [×10^5 kg]	2.15	2.20	2.25

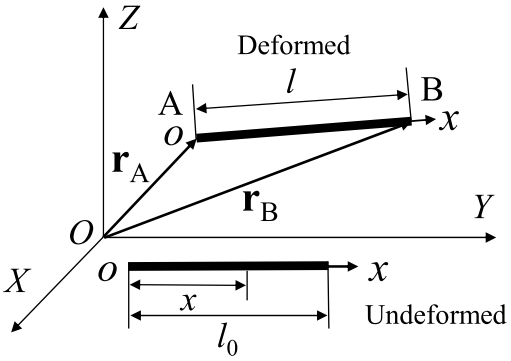

FIGURE 4. Expression of NPFEM element.

III. FORMULATION OF NONEQUATORIAL SPACE ELEVATOR BY NONLINEAR FEM

A. FORMULATION OF NONEQUATORIAL SPACE ELEVATOR IN NPFEM

The NPFEM proposed by Zhu *et al.* [23], [24] is a type of nonlinear FEM that considers geometric nonlinearities and can efficiently analyze the three-dimensional motion of objects with negligible bending stiffness such as tethers. Rigid-body motion and elastic deformation are coupled in the NPFEM. In this study, the tether was modeled as a stepped bar with a constant cross-sectional area within the element. The one-dimensional linear tether element is depicted in Fig. 4 in the absolute coordinate system *O–XYZ*, wherein the position vector $\mathbf{r}$ at any point on the x-axis of the element can be expressed as follows:

$$\mathbf{r} \equiv \begin{bmatrix} r_1 & r_2 & r_3 \end{bmatrix}^{\mathrm{T}}, \tag{2}$$

where r_1, r_2, and r_3 denote the X-, Y-, and Z-directional components of the position vector $\mathbf{r}$ at any point on the x-axis of the element. All these components are defined in the absolute coordinate system. As portrayed in Fig. 4, node A denotes the point at $x = 0$, whereas node B is at $x = l_0$, where l_0 denotes the natural length of the tether element. The length of the tether element after deformation is defined as $l \equiv \left|\mathbf{r}^{\mathrm{B}} - \mathbf{r}^{\mathrm{A}}\right|$, using the position vectors $\mathbf{r}^{\mathrm{A}}$ and $\mathbf{r}^{\mathrm{B}}$ of the nodes at both ends of the element in the absolute coordinate. $\mathbf{r}^{\mathrm{A}}$, $\mathbf{r}^{\mathrm{B}}$, and the ratio of l_0 and x provide an arbitrary position vector $\mathbf{r}$ in an element as

$$\mathbf{r} = (1-\xi)\,\mathbf{r}^{\mathrm{A}} + \xi \mathbf{r}^{\mathrm{B}}, \quad \mathbf{r} \equiv \mathbf{S}\mathbf{q}, \ \mathbf{q} \equiv \left[\left(\mathbf{r}^{\mathrm{A}}\right)^{\mathrm{T}} \left(\mathbf{r}^{\mathrm{B}}\right)^{\mathrm{T}} \right]^{\mathrm{T}}. \tag{3}$$

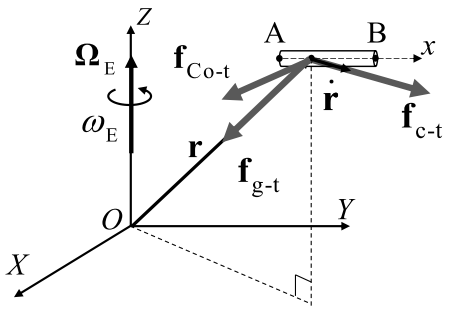

FIGURE 5. Gravitational force $\mathbf{f}_{g\text{-}t}$, centrifugal force vector $\mathbf{f}_{c\text{-}t}$, and Coriolis force vector $\mathbf{f}_{Co\text{-}t}$ acting on arbitrary point in element.

Note that $\xi \equiv x / l_0$. As shown in (3), a product of $\mathbf{S}$ and $\mathbf{q}$ yields an arbitrary position vector $\mathbf{r}$. The shape function $\mathbf{S}$ is a linear function shown in the appendix. The generalized coordinate vector $\mathbf{q}$ is composed of the global positions of the nodes at both ends of the element. Thus, the NPFEM offers six degrees of freedom per element. Moreover, the NPFEM described in an absolute coordinate can accurately represent the infinitesimal strains and large rotation motions.

$\mathbf{M}_t$, the mass matrix of each tether element, was derived from the kinetic energy K_t of the element, which can be written as

$$K_t \equiv \frac{1}{2}\int_0^{l_0} \rho A \dot{\mathbf{r}}^T \dot{\mathbf{r}}\, dx = \frac{1}{2}\dot{\mathbf{q}}^T \mathbf{M}_t \dot{\mathbf{q}}, \tag{4}$$

where ρ denotes the mass density of the tether element, and A indicates the cross-sectional area. The constant mass matrix $\mathbf{M}_t$ in NPFEM is highly advantageous for improving the computational efficiency of dynamic analysis.

The subsequent step is the derivation of the elastic force vector $\mathbf{Q}_{el\text{-}t}$ generated by the stretching deformation of the tether element. More specifically, $\mathbf{Q}_{el\text{-}t}$ was derived from the elastic energy $U_{el\text{-}t}$ of the element. The strain ε_x caused by the elongational deformation of the element in the x-axis direction is defined as

$$\varepsilon_x \equiv \frac{l}{l_0} - 1. \tag{5}$$

If the modulus of elasticity E and cross-sectional area A are not functions of x, the elastic potential energy $U_{el\text{-}t}$ in the direction of elongation of the tether element is expressed as

$$U_{el\text{-}t} \equiv \frac{1}{2} EA \int_0^{l_0} \varepsilon_x^2 dx. \tag{6}$$

The partial differentiation with the generalized coordinate $\mathbf{q}$ yields $\mathbf{Q}_{el\text{-}t}$ in a nonlinear form as

$$\mathbf{Q}_{el\text{-}t} \equiv \frac{\partial U_{el\text{-}t}}{\partial \mathbf{q}} = EA\left(\frac{1}{l_0} - \frac{1}{l}\right)\begin{bmatrix} -\left(\mathbf{r}^B - \mathbf{r}^A\right) \\ \mathbf{r}^B - \mathbf{r}^A \end{bmatrix}. \tag{7}$$

Subsequently, the generalized external force vector of the tether element was derived. If the gravitational, centrifugal, and Coriolis forces act on the tether element at arbitrary positions, as depicted in Fig. 5, each generalized force of the tether element $\mathbf{Q}_{g\text{-}t}$, $\mathbf{Q}_{c\text{-}t}$, and $\mathbf{Q}_{Co\text{-}t}$ can be derived based on the principle of virtual work as

$$\mathbf{Q}_{g\text{-}t} \equiv \int_0^{l_0} \mathbf{S}^T \mathbf{f}_{g\text{-}t} A dx, \quad \mathbf{f}_{g\text{-}t} \equiv -\mu\rho \frac{\mathbf{r}}{|\mathbf{r}|^3}, \tag{8}$$

$$\mathbf{Q}_{c\text{-}t} \equiv \int_0^{l_0} \mathbf{S}^T \mathbf{f}_{c\text{-}t} A dx, \quad \mathbf{f}_{c\text{-}t} \equiv \rho\omega_E^2\, \mathbf{r}|_{r_3^A, r_3^B = 0}^T, \tag{9}$$

$$\mathbf{Q}_{Co\text{-}t} \equiv \int_0^{l_0} \mathbf{S}^T \mathbf{f}_{Co\text{-}t} A dx, \quad \mathbf{f}_{Co\text{-}t} \equiv 2\rho\, \dot{\mathbf{r}} \times \mathbf{\Omega}_E, \tag{10}$$

where $\mathbf{f}_{g\text{-}t}$, $\mathbf{f}_{c\text{-}t}$, and $\mathbf{f}_{Co\text{-}t}$ represent the vectors of each force acting on any point in the element, respectively. μ denotes the geocentric constant, and ρ denotes the mass density. $\mathbf{\Omega}_E \equiv \begin{bmatrix} 0 & 0 & \omega_E \end{bmatrix}^T$ represents the angular velocity vector of the rotation of the Earth. According to Lagrange's equation, the equation of motion of a tether element can be written as

$$\mathbf{M}_t \ddot{\mathbf{q}} + \mathbf{Q}_{el\text{-}t} = \mathbf{Q}_{g\text{-}t} + \mathbf{Q}_{c\text{-}t} + \mathbf{Q}_{Co\text{-}t}. \tag{11}$$

The superposition of each element provides the equations of motion for all tether elements.

Furthermore, the counterweight was assumed as a lumped mass of m_{cw} located at the free end of the tether. The position vector of the counterweight is denoted as $\mathbf{r}_{cw}$, and the generalized coordinate vector of the counterweight element is denoted as $\mathbf{q}_{cw}$, which is equivalent to the generalized coordinate vector of the free end element of the tether. The kinetic energy of the counterweight K_{cw} can be defined as

$$K_{cw} \equiv \frac{1}{2}\dot{\mathbf{r}}_{cw}^T m_{cw} \dot{\mathbf{r}}_{cw} = \frac{1}{2}\dot{\mathbf{q}}_{cw}^T \mathbf{M}_{cw} \dot{\mathbf{q}}_{cw}. \tag{12}$$

Based on the principle of virtual work, the generalized gravitational force vector $\mathbf{Q}_{g\text{-}cw}$, generalized centrifugal force vector $\mathbf{Q}_{c\text{-}cw}$, and generalized Coriolis force vector $\mathbf{Q}_{Co\text{-}cw}$ acting on the counterweight can be derived as

$$\mathbf{Q}_{g\text{-}cw} \equiv -\mu m_{cw}\, \mathbf{S}|_{x=l_0}^T \frac{\mathbf{r}_{cw}}{|\mathbf{r}_{cw}|^3}, \tag{13}$$

$$\mathbf{Q}_{c\text{-}cw} \equiv m_{cw}\, \mathbf{S}|_{x=l_0}^T\, \mathbf{r}_{cw}|_{r_3^A, r_3^B = 0}\, \omega_E^2, \tag{14}$$

$$\mathbf{Q}_{Co\text{-}cw} \equiv 2m_{cw}\, \mathbf{S}|_{x=l_0}^T\, \dot{\mathbf{r}}_{cw} \times \mathbf{\Omega}_E. \tag{15}$$

Consequently, the equation of motion for the tether–counterweight system was obtained by superposing the mass matrix and generalized force vector for the counterweight with the element at the free end of the tether. The resulting equations of motion require considering boundary conditions at both tether ends. In this model, the end on the anchor side was a ball joint, whereas the end on the counterweight side was free. Hence, the equations of motion for the entire model considering the boundary conditions can be derived by eliminating the matrices representing the nodes with simple support conditions. Subsequently, the Newton–Raphson method was employed to conduct the static analysis of the equation of motion for the tether and counterweight of a nonequatorial space elevator. In equilibrium, $\ddot{\mathbf{q}} = \mathbf{0}$,

$\dot{\mathbf{q}} = \mathbf{0}$, and the equation of motion for the nonequatorial space elevator system can be written as

$$\mathbf{R}(\mathbf{q}) \equiv -\mathbf{Q}_{\text{el-t-all}} + \mathbf{Q}_{\text{g-t-all}} + \mathbf{Q}_{\text{c-t-all}} + \mathbf{Q}_{\text{g-cw}} + \mathbf{Q}_{\text{c-cw}} = \mathbf{0}, \tag{16}$$

where $\mathbf{R}(\mathbf{q})$ represents the residual force from the equilibrium position. The equilibrium position can be obtained when $\mathbf{R}(\mathbf{q}) = \mathbf{0}$. The partial differentiation of the left-hand side of (16) with the variable $\mathbf{q}$ yields the Jacobian matrix $\mathbf{J}$, and the equation to be solved can be stated as

$$\mathbf{J}\Delta\mathbf{q} = -\mathbf{R}(\mathbf{q}), \quad \mathbf{J} \equiv \frac{\partial \mathbf{R}(\mathbf{q})}{\partial \mathbf{q}}. \tag{17}$$

The solution of (17) considering the boundary conditions yields the modification $\Delta\mathbf{q}$. Upon updating the value of $\mathbf{q}$ until $\Delta\mathbf{q}$ is sufficiently small, the generalized coordinate vector $\mathbf{q}$ at the equilibrium position can be obtained as a solution of (16).

Moreover, the climber motion was formulated according to the method proposed by Sun *et al.* [30]. The position of the climber in the local coordinate system x_{cl} and the position and velocity vectors of the climber in the absolute coordinate system $\mathbf{r}_{\text{cl}}$ and $\dot{\mathbf{r}}_{\text{cl}}$ are illustrated in Fig. 6. In this paper, the upward motion of the climber was expressed as a temporal function in advance. The ascent operation of the climber was set to 1) acceleration, 2) constant speed, 3) deceleration, and 4) stop. In particular, the acceleration and deceleration in operations 1 and 3 can be expressed using trigonometric functions, and the ratio of acceleration and deceleration to the total ascent period was assumed as constant. The velocity of the climber in the local coordinate system $\dot{x}_{\text{cl}}$ was set as

$$\dot{x}_{\text{cl}} = \begin{cases} -\dfrac{v_{\text{r max}}}{2}\cos\left(\dfrac{2\pi}{T_{\text{climb}}}\right)t + \dfrac{v_{\text{r max}}}{2} \\ \qquad \left(0 \le t \le \dfrac{T_{\text{climb}}}{2}\right) \\ v_{\text{r max}} \\ \qquad \left(\dfrac{T_{\text{climb}}}{2} \le t \le \dfrac{2 - N_{\text{rate}}}{2N_{\text{rate}}} T_{\text{climb}}\right) \\ -\dfrac{v_{\text{r max}}}{2}\cos\left(\dfrac{2\pi}{T}\right)t + \dfrac{v_{\text{r max}}}{2} \\ \qquad \left(\dfrac{2 - N_{\text{rate}}}{2N_{\text{rate}}} T_{\text{climb}} \le t \le \dfrac{T_{\text{climb}}}{N_{\text{rate}}}\right) \\ 0 \\ \qquad \left(t \ge \dfrac{T_{\text{climb}}}{N_{\text{rate}}}\right), \end{cases} \tag{18}$$

where t denotes time. x_{cl} and $\ddot{x}_{\text{cl}}$ can be evaluated by first-order integration and differentiation. considering the continuity of the function. Therefore, the ascent plan of the climber can be determined by setting the ascent period T_{climb}, the maximum relative velocity of the climber v_{rmax}, and the time ratio of acceleration and deceleration to the total ascent period N_{rate}.

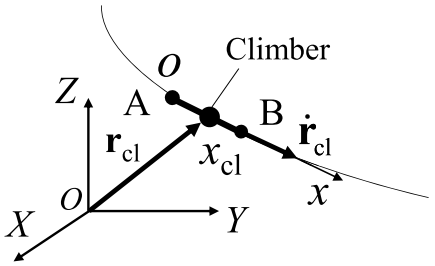

FIGURE 6. Climber position in local coordinate system x_{cl}, climber position vector $\mathbf{r}_{\text{cl}}$, and velocity vector $\dot{\mathbf{r}}_{\text{cl}}$ in absolute coordinate system.

B. FORMULATION OF EQUATIONS OF MOTION FOR ENTIRE SYSTEM OF SPACE ELEVATOR

In this paper, the space elevator system is defined as containing a tether, counterweight, and climber. Accordingly, the equations of motion for the entire space elevator system can be obtained by incorporating the mass matrix, generalized external force vector, and the constraint equation with respect to the climber into the equations of motion for the tether and counterweight. The generalized coordinate vector $\mathbf{q}_{\text{entire}}$ for the entire system is defined as follows:

$$\mathbf{q}_{\text{entire}} \equiv \begin{bmatrix} \mathbf{q}_{\text{t-all}} \\ x_{\text{cl}} \end{bmatrix}, \tag{19}$$

where $\mathbf{q}_{\text{t-all}}$ represents the generalized coordinate vector which is superposed all tether elements. The mass matrix and the generalized force vectors of the climber must be placed appropriately in the equation of motion of the entire space elevator system. The mass matrix of the entire space elevator system $\mathbf{M}_{\text{entire}}$ was obtained as follows:

$$\mathbf{M}_{\text{entire}} \equiv \begin{bmatrix} \mathbf{M}_{\text{t-all}} + \mathbf{M}_{\text{cw}} & \mathbf{0} \\ \mathbf{0} & 0 \end{bmatrix} + \mathbf{M}_{\text{cl}}, \tag{20}$$

where $\mathbf{M}_{\text{t-all}}$, $\mathbf{M}_{\text{cw}}$, and $\mathbf{M}_{\text{cl}}$ represent the mass matrices of all the tether elements, counterweight, and climber, respectively. Similarly, the generalized force vector for the entire space elevator system $\mathbf{Q}_{\text{entire}}$ was obtained by rearranging the generalized force vectors for the tether, counterweight, and climber to the size of the entire system and adding them together. In addition, the constraint equations for the climber and tether were introduced by solving the equations of motion of the entire space elevator system, including the climber, tether, and counterweight. Therefore, the equation of motion of the entire space elevator system required to be solved can be stated as

$$\mathbf{M}_{\text{entire}}\ddot{\mathbf{q}}_{\text{entire}} = \mathbf{Q}_{\text{entire}} + \begin{bmatrix} \mathbf{0} \\ \gamma \end{bmatrix}. \tag{21}$$

γ represents the second-order time derivative of the constraint equation for the climber. In the simulation, x_{cl}, $\dot{x}_{\text{cl}}$, and $\ddot{x}_{\text{cl}}$ of the climber in each step were input to evaluate γ in advance.

IV. ANALYSIS RESULTS AND DISCUSSION

A. ANALYSIS BY PROPOSED NPFEM

The NPFEM model formulated in the previous section was used to obtain the equilibrium position of a nonequatorial

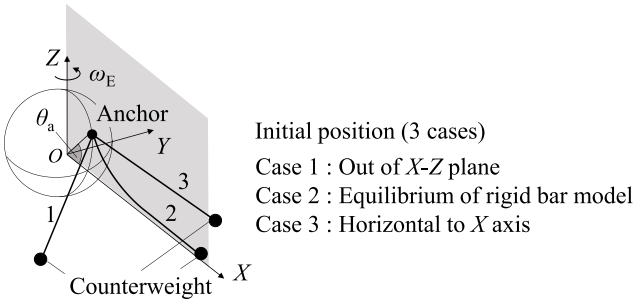

FIGURE 7. Initial position in static analysis (3 cases).

space elevator based on the Newton–Raphson method to perform the dynamic analysis during climber ascent. In this paper, three anchor latitudes θ_a were selected, namely, 0°, 15°, and 20°. The anchor longitude φ_a was assumed as 0° to ensure the position of the anchor in the X–Z plane. The three cases, given as the initial position of the tether in the static analysis, are illustrated in Fig. 7. Case 1 displays the initial position of the tether in the instance it is situated outside the X–Z plane, including the rotation axis and anchor. Case 2 exhibits the equilibrium position obtained from the rigid bar model, and Case 3 depicts the initial position horizontal to the X-axis. In Cases 2 and 3, the tether Y-direction component at any given position was zero. Initially, each element was stretched by $\varepsilon_0 \equiv \sigma_a / E$, and the total number of elements N_{ele} was set to 100. Summarily, the parameters of the analysis are listed in Table 2. In this section, the cross-sectional area of each element was expressed as the tapered cross-sectional area value obtained in Section II.

First, a static analysis was performed at an anchor latitude θ_a of 20° with the counterweight mass values obtained from the rigid bar model. However, the solution did not converge owing to the elongation deformation of the models. Thus, we adjusted the mass of the counterweight to converge the solution. In the following analysis, the counterweight mass was set to 2.68×10^5 kg, which is 120% of the value obtained from the rigid bar model. In Case 1, the initial position is expressed outside the plane, including the rotation axis and anchor. The proposed NPFEM model holds a three-dimensional Cartesian coordinate system, which can assume the initial positions as Case 1 that do not fit in a two-dimensional plane used in the rigid bar model. Nevertheless, as depicted in Fig. 8, the equilibrium position was obtained in the plane containing the rotation axis and anchor, even if the initial position was located outside this plane. This was because the gravitational gradient torque acted on the tether outside the plane containing the rotation axis and anchor. In the static analysis of this paper, the force acted only in the direction of the line connecting the point of force action and origin. In all instances, the anchor position of the space elevator was constrained to a point on the Earth. Therefore, the equilibrium position was in the plane containing the anchor and rotation axis, except for considering the

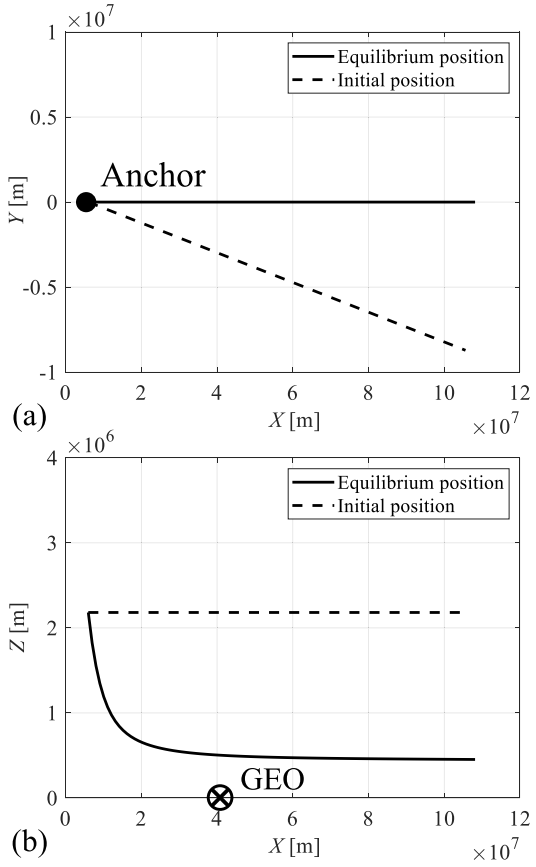

FIGURE 8. (a) Equilibrium position viewed in $X - Y$ plane; (b) Equilibrium position viewed in $X - Z$ plane with Case 1 (Note that the scale of the vertical axis varies from that of the horizontal axis.)

disturbances acting outside this plane. In Cases 2 and 3, the equilibrium positions converged to the same value as that displayed in Fig. 8. Therefore, the three cases assumed in this paper could be deemed to have no initial-value dependency.

The results of the static analysis from the X–Z plane, including the rotation axis and the anchor, are depicted in Fig. 8, which demonstrated that the equilibrium position of the nonequatorial space elevator was curved toward the center of the Earth near the Earth and followed the equatorial plane as it moved toward deep space. This was because the gravitational force acted toward the origin near the surface of the Earth, whereas the centrifugal force acted positively in the X–Y plane (Fig. 2). In addition, the space elevator was approximately 5.0×10^5 m higher than the GEO in the Z-axis direction. Thus, the equilibrium position of the nonequatorial space elevator could effectively avoid collisions with spacecraft in the GEO.

Subsequently, the dynamic responses of the tether during climber ascent were analyzed, considering the equilibrium position obtained in the static analysis as the initial position. The classical fourth-order Runge–Kutta method with four stages was adopted as the calculation scheme, the time interval was set to 1.0 s. The climber mass was set to 1.0×10^3 kg. The maximum relative velocity of the climber v_{rmax} was set

TABLE 2. Present analysis parameters.

Material density	[kg/m^3]	ρ	1.30×10^3
Modulus of longitudinal elasticity	[GPa]	E	1.00×10^3
Anchor cross-sectional area	[m^2]	A_a	1.00×10^{-5}
Allowable stress	[GPa]	σ_a	2.00×10^1
Overall length of tether	[m]	–	1.00×10^8
Natural length of tether element	[m]	l_0	1.00×10^6
Anchor latitude	[deg]	θ_a	2.00×10^1
Anchor longitude	[deg]	φ_a	0
Counterweight mass obtained by rigid-bar model ($\theta_a = 20°$)	[kg]	m_{cw}	2.68×10^5
Convergence threshold	[N]	–	1.00×10^{-7}
Number of elements	[–]	N_{ele}	2.00×10^2
Number of iterations of Newton-Raphson method	[–]	–	1.00×10^3

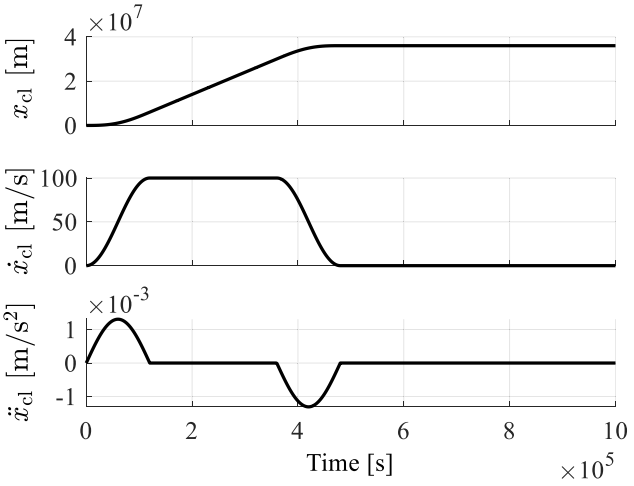

FIGURE 9. Time history of climber altitude, velocity, and acceleration.

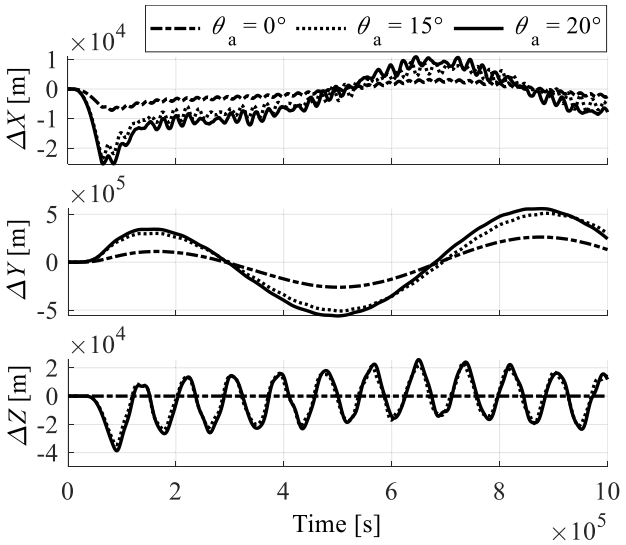

FIGURE 10. Time history of tether free end at each latitude.

at 100 m/s for the ascent period T_{climb}, and the time ratio of acceleration and deceleration to constant-speed operation period N_{rate} was set as 0.5. The time histories of the altitude, velocity, and acceleration of the climber at each time interval are presented in Fig. 9, which were utilized in further analyses.

The displacement of the free end of the tether at latitudes 0°, 15°, and 20° are comparatively presented in Fig. 10, which reflects the displacement of the free end of the tether from its equilibrium position during climber ascent. Overall, the displacement in the X-direction was observed at every anchor latitude owing to the tension variation caused by the climber ascent. Specifically, the displacement magnitude ranged from -2.5×10^4 to $+1.0 \times 10^4$ m, which is within the range of small deformations compared with the total tether length of 1.0×10^8 m. In addition, a high anchor latitude results in a large displacement, potentially because a high anchor latitude causes a more significant variation in the tension.

In the Y-direction, oscillations of approximately $+5 \times 10^5$ m were observed, and its period and amplitude were larger compared to those of the oscillations in the remaining directions. The Coriolis force caused by the stretching motion of the tether and the upward motion of the climber caused this oscillation. Although the Coriolis force causes oscillation in the negative Y-direction as the climber ascends, the displacement in this analysis was observed in the positive direction. This was probably owing to the more dominant Coriolis force resulting from the elongation deformation of the tether than the climber ascent for the given parameters.

The displacement in the Z-direction was observed only at the anchor latitude was situated in the nonequatorial area because the combined force vector of the gravitational and centrifugal forces included a component outside the X–Y plane at the nonequatorial latitude, as displayed in Fig. 2. These oscillations had shorter periods and smaller amplitudes than in the Y-direction. Based on these results, the Y-direction oscillation can be deemed the most dominant oscillation during climber ascent.

The elongation rate of each element (defined as l / l_0) at equilibrium is presented in Fig. 11(a), which indicates the nonuniform stress acting on each element. Thus, the stress acting on the NPFEM is not necessarily uniform, regardless of the constant stress acting on the rigid bar of the tapered cross-sectional area (Fig. 3). The immense stress was shown in the elements constrained to the anchor because the enormous centrifugal force pulled the tether in a higher orbit. As the NPFEM model considers the elongation deformation of each element, the results discussed above were obtained for the cross-sectional area set by the rigid bar model. In future, a method should be developed to determine the optimal taper shape required for maintaining constant stress, even in nonlinear finite element models such as NPFEM. The time history of the variations in each element length is illustrated in Fig. 11(b), depicting that the proposed method displayed a stretching deformation of the elements that is not observed under the conventional rigid bar model [20].

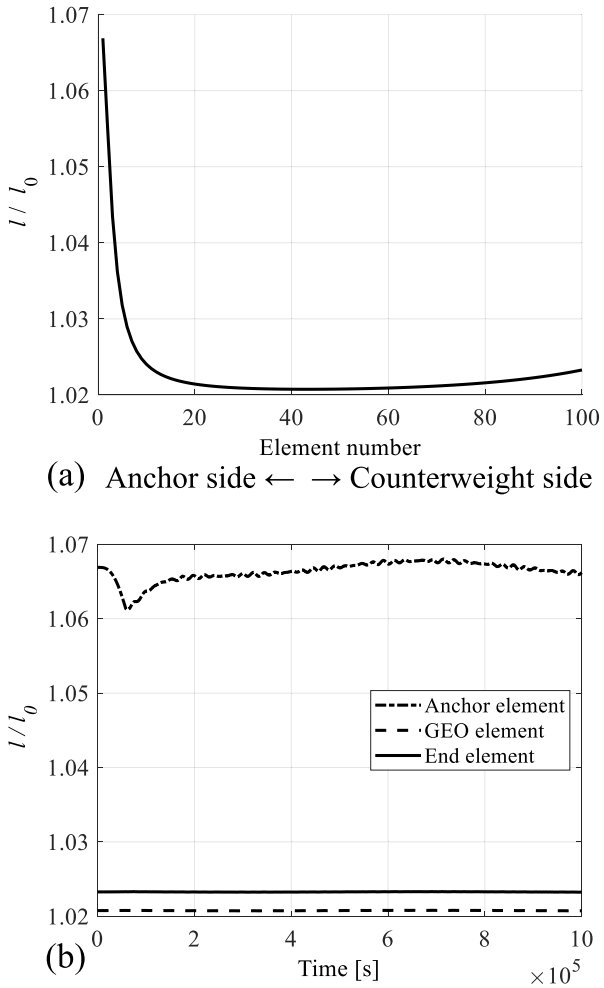

FIGURE 11. (a) Elongation rate of each element at equilibrium state; (b) Time history of elongation rate of each element in dynamic analysis.

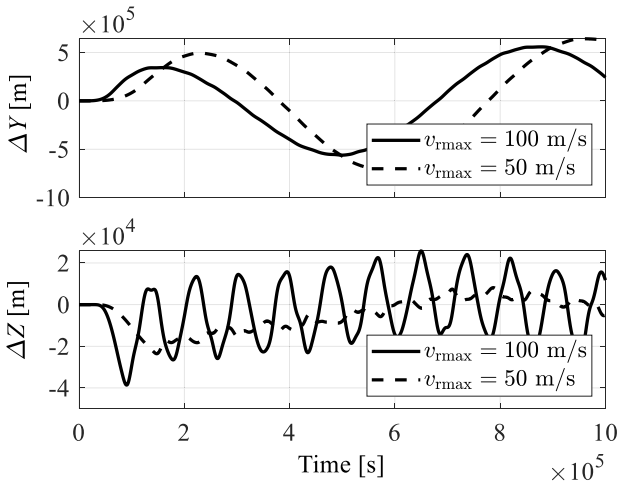

FIGURE 12. Comparison of climber maximum relative velocity $v_{rmax} = 50$ and 100 m/s.

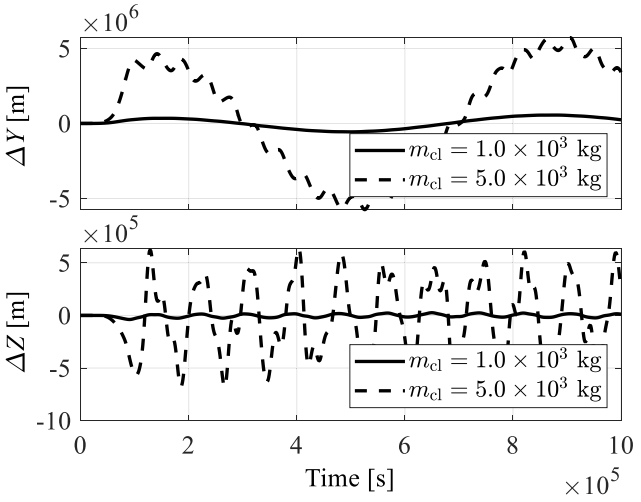

FIGURE 13. Comparison of climber mass $m_{cl} = 1.0 \times 10^3$ and 5.0×10^3 kg.

More importantly, the variation in the elongation rate was more pronounced for the element connected to the anchor than for the element at the free end with GEO. Focusing on the element connected to the anchor, a temporary reduction in the elongation rate was observed at $t = 5 \times 10^4$ s, which signified that the element connected to the anchor experienced slackening from the initial tensile state (as the elongation rate > 1, it was still in tension). This phenomenon was caused by the movement of a climber from one tether element to the other, which unloaded the tether element at the location of the climber. According to the relationship between the combined gravitational and centrifugal forces at each altitude (Fig. 2), this phenomenon was particularly prominent when the climber was situated in the near-Earth region.

B. RESULT COMPARISONS IN VARIOUS CONDITIONS

Furthermore, the dynamic characteristics of the space elevator for various maximum relative velocities of the climber v_{rmax} are illustrated in Fig. 12. As observed, the dynamic effect of the tether decreased with the constant velocity of the climber, which was consistent with the characteristics reported in prior research [16]. This was because the energy of the tether-counterweight system, provided by the climber motion, was reduced. The dynamic responses of the tether under various masses of the climber are comparatively presented in Fig. 13, which implies that the dynamic response increased with the climber mass, as consistent with the reports of previous studies [16]. The influence of varying the initial climber acceleration on the dynamic response of the tether is depicted in Fig. 14, wherein both the cases accelerated to $v_{rmax} = 100$ m/s. In two cases, the ratio of the acceleration time to constant speed ascent time was $N_{rate} = 0.5$ and 0.01. For gradual acceleration, i.e., $N_{rate} = 0.5$, the oscillation period was larger, and the amplitude was smaller than those at $N_{rate} = 0.01$, implying that the dynamic response to the tether was suppressed for lower acceleration. These results indicate that the larger the payload mass or, the shorter the overall transport time and acceleration time, the more difficult it is

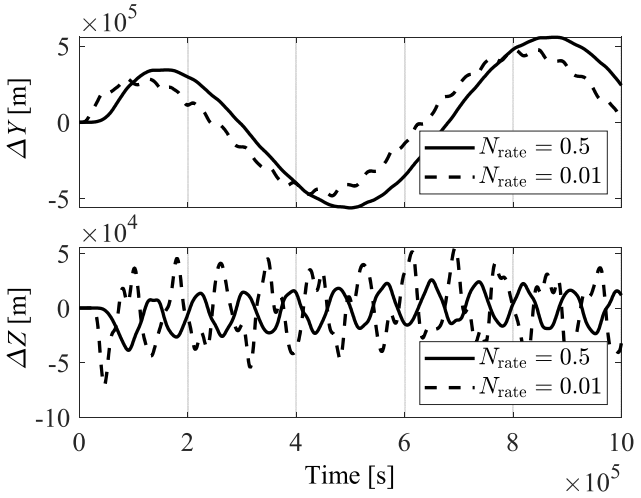

FIGURE 14. Comparison of dynamic response of tether with various acceleration time of climber (N_{rate} is ratio of acceleration time to constant speed ascent time).

to control the oscillation of the space elevator. In addition, the robustness of the proposed method was verified. When the input was altered, the calculation did not diverge.

C. VERIFICATION BY COMPARISON WITH CONVENTIONAL METHOD

The validity of the nonequatorial space elevator theory based on the nonlinear FEM described thus far was verified by comparing its results with those obtained using the conventional method [20], [21]. Although the conventional method [20], [21] analyzed a spring-mass model (1000 elements) with a time step of 0.05 s, this study analyzed the proposed NPFEM model (100 elements) with a time step of 1.0 s. The parameters other than those mentioned above were aligned with those reported by Wang *et al.* [21]. The comparison results are displayed in Fig. 15. The static results presented in Fig. 15(a) indicate that the proposed NPFEM had a larger equilibrium position in the X-direction than the conventional model [21] because the proposed NPFEM considered geometric nonlinearity and appeared a tensioned shape against the force originating from the gravitational field owing to its high stiffness. Thus, the geometric nonlinearity of the proposed NPFEM allowed the nonequatorial space elevator to avoid the high-concentration area of cosmic radiation to a greater extent than earlier. The time histories of the Y- and Z-direction displacements of the free end of the tether after the climber motion ceased are depicted on Fig. 15 (b) and (c). The Z-direction displacement obtained with the NPFEM was consistent with the conventional model [21]. However, the Y-direction displacement of the NPFEM was more significant than that of the conventional model [21] because the space elevator modeled by the NPFEM was more rigid and tensioned owing to the considered geometric nonlinearity. Consequently, the X-direction component at the

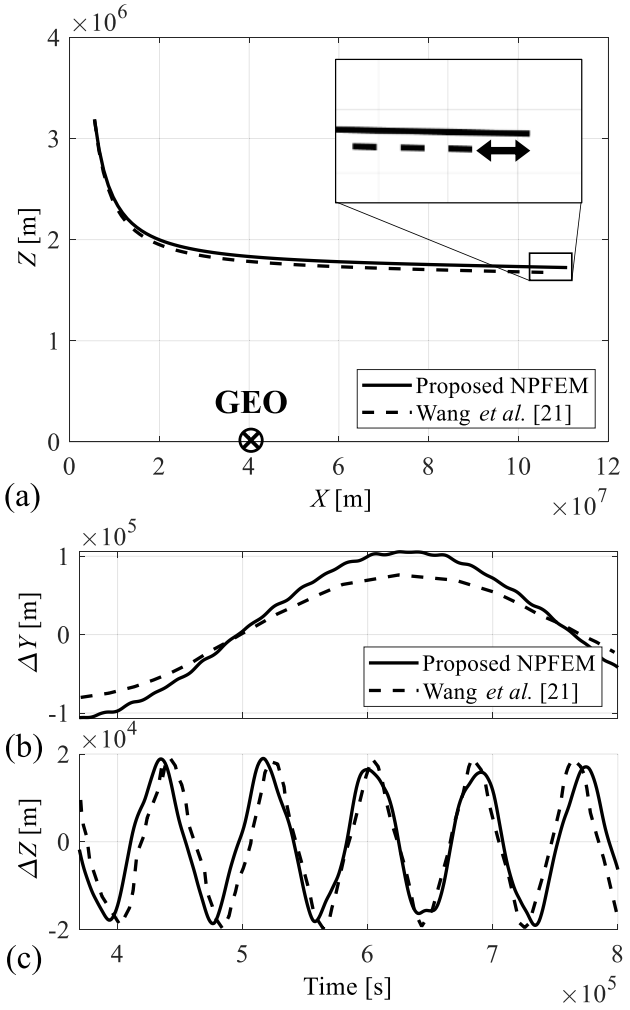

FIGURE 15. (a) Comparison of equilibrium position between proposed NPFEM and conventional model [21], comparison of displacements of tether free end during climber ascent; (b) Y-direction; (c) Z-direction (Note that the scales of vertical and horizontal axes are different.)

free end and the amplitude of the pendulum motion were larger in the NPFEM model, as indicated in Fig. 16.

D. ENERGY EXCHANGE BETWEEN COMPONENTS

1) ASSUMPTIONS OF SYSTEM

The energy analysis results of the nonequatorial space elevator are described herein. The energy analysis was conducted owing to two specific reasons: to validate the proposed model and discuss the energy aspects of nonequatorial space elevators in detail. The assumptions are summarized as follows.

1) The ''nonequatorial space elevator system'' comprises a tether, climber, and counterweight. The exterior of the system includes outer space, Earth, and the power system of the climber.
2) Based on a thermodynamic perspective, the ''nonequatorial space elevator system'' is an ''insulating system'' in which the energy transfer with the outside world occurs only through mechanical work (actual space

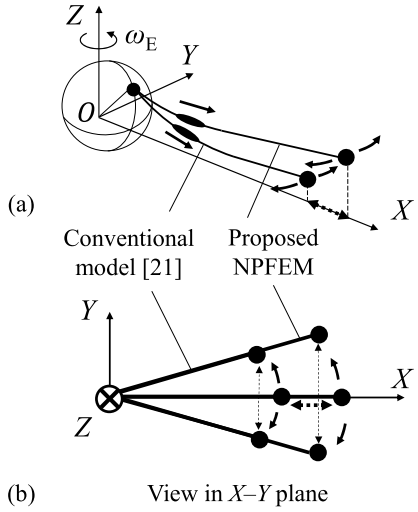

FIGURE 16. Qualitative comparison of oscillation between previous study [21] and proposed model (a) 3D schematic diagram, (b) X–Y plane schematic diagram.

elevators can be assumed to exchange heat with the outside world, but in this analysis, no heat was assumed to be transferred).

In the following discussion, we classify a "nonequatorial space elevator system" into two categories: 1) climber, 2) tether–counterweight, and consider the energy exchange for the components. Components 1 and 2 are coupled systems; therefore, the energy is not independently conserved in each system.

2) RESULT AND DISCUSSION

The energy of the entire system can be calculated using the following equations:

$$\begin{aligned}
K_{\text{entire}} &\equiv K_{\text{t-all}} + K_{\text{cw}} + K_{\text{cl}},\\
K_{\text{t-all}} &\equiv \sum_{i=1}^{N_{\text{ele}}} K_{\text{t-}i\text{th}}, \quad K_{\text{cw}} \equiv \frac{1}{2} m_{\text{cw}} \dot{\mathbf{r}}_{\text{cw}}^{\text{T}} \dot{\mathbf{r}}_{\text{cw}},\\
K_{\text{cl}} &\equiv \frac{1}{2} m_{\text{cl}} \dot{\mathbf{r}}_{\text{cl}}^{\text{T}} \dot{\mathbf{r}}_{\text{cl}}, \qquad (22)\\
U_{\text{entire}} &\equiv U_{\text{t-all}} + U_{\text{cw}} + U_{\text{cl}},\\
U_{\text{t-all}} &\equiv U_{\text{el-t-all}} + U_{\text{g-t-all}} + U_{\text{c-t-all}},\\
&\equiv \frac{1}{2} \mathbf{Q}_{\text{el-t-all}}^{\text{T}} \mathbf{q}_{\text{t-all}} + \mathbf{Q}_{\text{g-t-all}}^{\text{T}} \mathbf{q}_{\text{t-all}} - \frac{1}{2} \mathbf{Q}_{\text{c-t-all}}^{\text{T}} \mathbf{q}_{\text{t-all}},\\
U_{\text{cw}} &\equiv U_{\text{g-cw}} + U_{\text{c-cw}} \equiv -\frac{\mu m_{\text{cw}}}{|\mathbf{r}_{\text{cw}}|} - \frac{1}{2} m_{\text{cw}} \omega_{\text{E}}^2 \mathbf{r}_{\text{cw}}^{\text{T}} \mathbf{r}_{\text{cw}},\\
U_{\text{cl}} &\equiv U_{\text{g-cl}} + U_{\text{c-cl}} \equiv -\frac{\mu m_{\text{cl}}}{|\mathbf{r}_{\text{cl}}|} - \frac{1}{2} m_{\text{cl}} \omega_{\text{E}}^2 \mathbf{r}_{\text{cl}}^{\text{T}} \mathbf{r}_{\text{cl}}. \qquad (23)
\end{aligned}$$

In this section, the analysis results in Section IV-A are used for discussion.

The time history of the total energy of the space elevator system—the sum of the total energy of the tether, counterweight, and climber—is presented in Fig. 17. The total energy of the space elevator system increased with the ascent of the climber and thereafter remained almost constant. The total

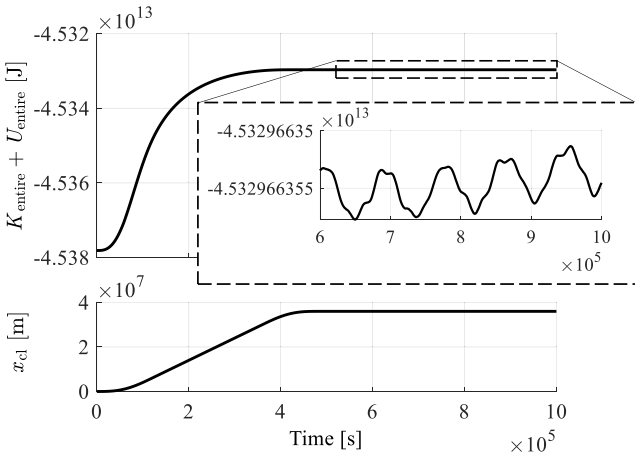

FIGURE 17. Total energy history of nonequatorial space elevator system (upper panel) and position history of climber (lower panel).

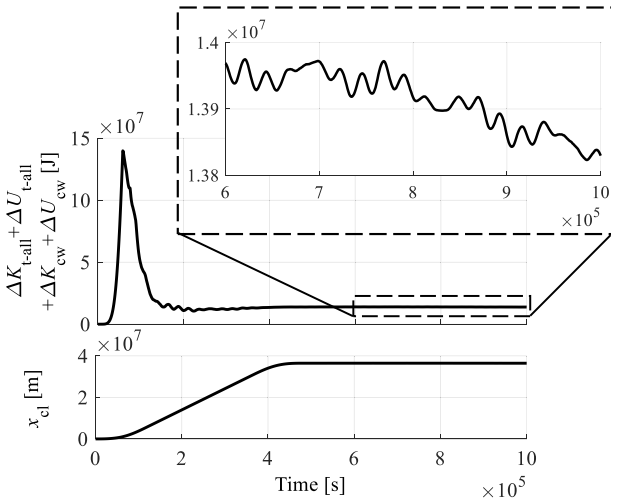

FIGURE 18. Total energy history of tether–counterweight system (upper panel) and position history of climber (lower panel).

energy of the space elevator system after the termination of the ascent exhibited a relative variation of 10^{-9}; thus, it was well conserved. In conclusion, the proposed method was verified in terms of energy conservation.

The time history of the energy fluctuation of the tether–counterweight system is depicted in Fig. 18. A sudden increase in energy was observed at 0–1.0 $\times$ 10^5 s after the climber started to ascend. After that, the total energy of the tether–counterweight system decreased. The same phenomenon occurred for an anchor latitude of 0°. This phenomenon can be explained by the climber ascent causing the tension variation in the tether. Specifically, it can be considered that the tether deformation varied the climber position in absolute coordinate and transferred energy to the climber. Afterward, the total energy fluctuated at approximately 1.4 $\times$ 10^7 J, owing to the climber motion associated with the tether oscillation. The tether–counterweight energy

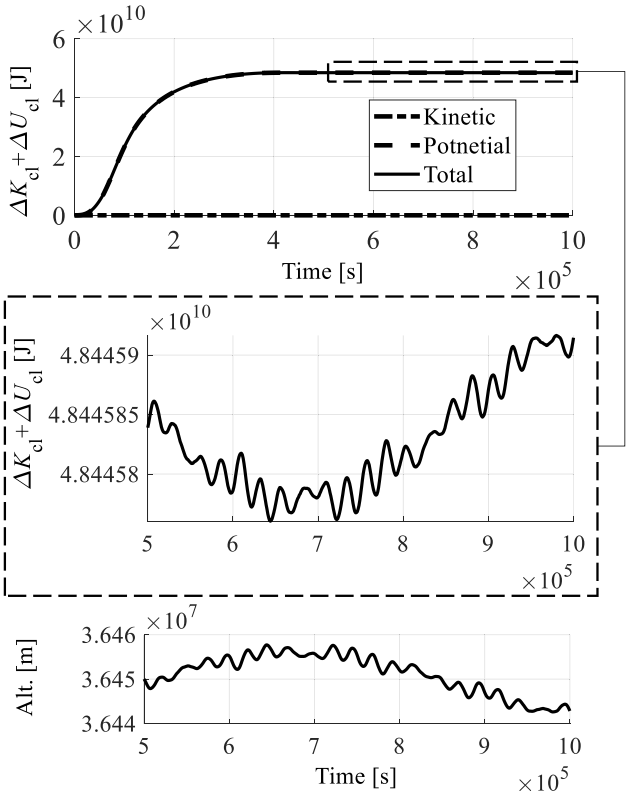

FIGURE 19. Energy history of climber (upper, middle panel) and altitude variation of climber (lower panel) after ascent termination.

fluctuation after the climber ascent was on the order of 10^5 J, as depicted in Fig. 18.

On the other hand, the climber energy fluctuation after the climber ascent was also on the order of 10^5 J, as depicted in Fig. 19. The climber motion associated with the tether oscillation was approximately $\pm 1.0 \times 10^4$ m oscillation centered at an altitude of the GEO (Fig. 19, lower panel). For instance, the fluctuation of potential energy $\Delta(U_{g-cl} + U_{c-cl})$ is calculated as approximately 1.0×10^5 J when a climber moves 1.0×10^4 m toward the Earth at the GEO. Considering that the potential energy was more dominant than the kinetic energy in this analysis, this theoretical calculation result is equivalent to the order of the energy fluctuation observed in the middle panel of Fig. 19; it represents the physical phenomenon of the climber motion associated with the tether motion, not a numerical error. Therefore, the energy exchange between the tether–counterweight system and the climber after the climber ascent could be on the order of 10^5 J.

TABLE 3. Variations in energy before and after climber ascent energy at initial time $t = 0$ s was assumed as zero. Unit is [J].

	Tether and counterweight	Climber
Kinetic energy	3.23×10^5	1.83×10^3
Potential energy of combined gravitational and centrifugal field	1.39×10^9	4.84×10^{10}
Elastic potential energy	-1.39×10^9	–
Total energy	1.39×10^7	4.84×10^{10}

Subsequently, the energy exchange of the space elevator during climber ascent was analyzed by classifying components into the tether–counterweight system and the climber. Table 3 summarizes the energy changes of each component when comparing the initial time $t = 0$ s and the end of climber ascent $t = 4.8 \times 10^5$ s. Focusing on the total energy in Table 3, the increase to 4.84×10^{10} J in the climber system and 1.39×10^7 J in the tether–counterweight system could observe at the end of the climber ascent. The energy increase in the tether–counterweight system corresponds to the energy transferred from the climber. Moreover, the tether–counterweight system continued to oscillate even after the termination of the climber ascent. As the climber was modeled assuming that it is located on the tether at all instances, the climber moved with the tether oscillation even after its ascending operation stopped. Consequently, this motion caused energy transfer from the tether–counterweight system to the climber system.

In summary, the energy exchange depicted in Fig. 20 was deemed to occur. The space elevator system receives energy from the power system and utilizes it for the climber ascent and oscillation of the system. In the space elevator system, the climber directly receives energy from the power system and transfers the energy to the tether–counterweight system.

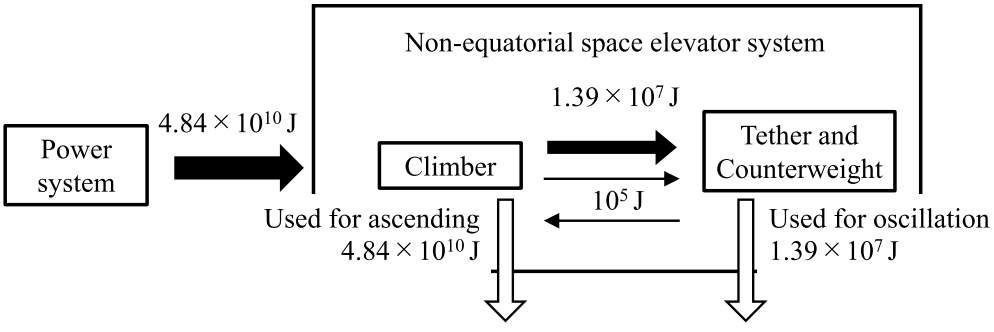

FIGURE 20. Schematic of energy exchange in entire system.

Overall, the climber and tether–counterweight system transfer energy to each other on the order of 10^5 J. In this paper, the low-order values did not precisely correspond because the order range of the values included in this analysis is large, and the influences of digit loss and rounding errors were more pronounced for low-order values (16 digits are retained in MATLAB).

V. CONCLUSION

The analysis model for space elevators proposed in this paper is more continuous than the conventional one and considers elongation deformation in the elements. The conventional models were formulated in terms of rigid bars [10], [20] and spring-mass elements [21]. The conventional model [21] did not consider the geometric nonlinearity of the tether, and this study enabled us to consider the geometric nonlinearities and analyze the coupling effect between rigid-body motion and elastic deformation of the tether. Furthermore, we formulated NPFEM in a rotational coordinate system, whereas conventional NPFEMs were formulated only in inertial coordinate systems. Subsequently, the established model developed a consistent analysis method for nonequatorial space elevators. This method includes deriving the complex equilibrium position of the nonequatorial space elevator using the iteration method as well as conducting dynamic analysis during the climber motion.

The static analysis results revealed that the equilibrium position of the tether was less inclined toward the center of the Earth than in the conventional model [20], [21]. As observed, the tether assumed a more tensioned equilibrium position than in the conventional model owing to the consideration of geometric nonlinearity. The proposed method provided more insights toward discussing debris collisions and avoiding the high radiation area of cosmic rays in nonequatorial space elevators. Owing to the difference of equilibrium positions, the displacement obtained from the dynamic analysis was larger in the Y-direction than in the conventional model.

In addition, we formulated the tether as an NPFEM model in a rotational coordinate system, which can consider the deformation of each tether element. Consequently, the stretching motion of the tether during the climber ascent and the motion of the entire system caused by the Coriolis force could be observed. This dynamic analysis demonstrated that a higher anchor latitude produces a larger overall displacement. Moreover, the displacement in the Z-direction was observed only when the anchor was located at a nonequatorial position. Although the nonequatorial space elevator displays attractive features such as avoiding debris collisions in GEO and high radiation of cosmic rays, its dynamic behavior is complicated. Therefore, these trade-offs must be carefully evaluated when considering suitable construction locations.

In this paper, the climber velocity, counterweight mass, and ascent function were varied, and accordingly, the feasibility of the nonequatorial space elevator varied under multiple conditions. Furthermore, the proposed method was validated to be stable for inputs with large displacements. The results of the parametric study displayed that the dynamic response of the nonequatorial space elevator increased with the climber velocity, acceleration, and mass.

Additionally, we analyzed the energy exchange between the components and discussed the results. It includes verifying the proposed model and a deeper discussion on the energy aspects of nonequatorial space elevators. The energy analysis results clarified the energy exchange between the components during the climber ascent. This study further explained the tension variations caused by the climber motion from an energy transfer perspective.

In future, a more accurate model that includes the torsional deformation of the tether and further coupling with the climber will be required. Future studies should focus on deriving an optimal cross-sectional shape experiencing constant stress in a nonlinear FEM and conducting a safety analysis of long tethers based on collision probability with space debris [39]–[41].

APPENDIX
MATRIX DEFINITION

The shape function $\mathbf{S}$ is expressed as

$$\mathbf{S} \equiv \begin{bmatrix} (1-\xi)\,\mathbf{I}_{3\times3} & \xi\mathbf{I}_{3\times3} \end{bmatrix}. \tag{A.1}$$

If cross-sectional area A and mass density ρ are not functions of x, the mass matrix of the tether $\mathbf{M}_\mathrm{t}$ can be expressed as

$$\mathbf{M}_\mathrm{t} \equiv \int_0^{l_0} \rho A \mathbf{S}^\mathrm{T}\mathbf{S}\,\mathrm{d}x = \frac{\rho A l_0}{6}\begin{bmatrix} 2\mathbf{I}_{3\times3} & \mathbf{I}_{3\times3} \\ \mathbf{I}_{3\times3} & 2\mathbf{I}_{3\times3} \end{bmatrix}. \tag{A.2}$$

Based on the perspective of kinetic energy, the mass matrix of the counterweight $\mathbf{M}_\mathrm{cw}$ is obtained in the form of a constant matrix as

$$\mathbf{M}_\mathrm{cw} \equiv \mathbf{S}|_{x=l_0}^\mathrm{T}\, m_\mathrm{cw}\, \mathbf{S}|_{x=l_0} = m_\mathrm{cw}\begin{bmatrix} \mathbf{O}_{3\times3} & \mathbf{O}_{3\times3} \\ \mathbf{O}_{3\times3} & \mathbf{I}_{3\times3} \end{bmatrix}. \tag{A.3}$$

REFERENCES

[1] Y. Artsutanov, *To the Cosmos by Electronic Train. (English Translation From Russian Original)*. Moscow, Russia: Komsomolskaya Pravda, Jul. 1960.
[2] J. Pearson, "The orbital tower: A spacecraft launcher using the Earth's rotational energy," *Acta Astronaut.*, vol. 2, nos. 9–10, pp. 785–799, Sep./Oct. 1975, doi: 10.1016/0094-5765(75)90021-1.
[3] S. Iijima, "Helical microtubules of graphitic carbon," *Nature*, vol. 354, pp. 56–58, Nov. 1991, doi: 10.1038/354056a0.
[4] D. V. Smitherman, "Space elevators: Building a permanent bridge for space exploration and economic development," in *Proc. AIAA Space Conf. Expo.*, Sep. 2000, pp. 1–9.
[5] B. C. Edwards, "Design and deployment of a space elevator," *Acta Astronaut.*, vol. 47, no. 10, pp. 735–744, Nov. 2000, doi: 10.1016/S0094-5765(00)00111-9.
[6] S. S. Cohen and A. K. Misra, "Elastic oscillations of the space elevator ribbon," *J. Guid., Control, Dyn.*, vol. 30, no. 6, pp. 1711–1717, Nov. 2007, doi: 10.2514/1.29010.
[7] S. Cohen and A. K. Misra, "Static deformation of space elevator tether due to climber," *Acta Astronautica*, vol. 111, pp. 317–322, Jun. 2015, doi: 10.1016/j.actaastro.2015.02.017.
[8] B. Gassend, "Non-equatorial uniform-stress space elevators," in *Proc. 3rd ISEC*, Washington, DC, USA, 2004, pp. 1–10.
[9] A. M. Jorgensen, S. E. Patamia, and B. Gassend, "Passive radiation shielding considerations for the proposed space elevator," *Acta Astronautica*, vol. 60, no. 3, pp. 198–209, Feb. 2007, doi: 10.1016/j.actaastro.2006.07.014.

[10] F. Cowan and J. Leonard, "A Mars colonization approach," in *Proc. AIAA SPACE Conf. Expo.*, Sep. 2007, pp. 1–17.
[11] N. Takeichi, "Geostationary station keeping control of a space elevator during initial cable deployment," *Acta Astronautica*, vol. 70, pp. 85–94, Jan. 2012, doi: 10.1016/j.actaastro.2011.07.016.
[12] K. Tao, Y. Yamagiwa, K. Otsuka, and Y. Ishikawa, "Study about the simultaneous deployment performance of the cables from GEO station at the space elevator construction," *Acta Astronautica*, vol. 138, pp. 590–595, Sep. 2017, doi: 10.1016/j.actaastro.2017.01.032.
[13] V. S. Aslanov, A. S. Ledkov, A. K. Misra, and A. D. Guerman, "Dynamics of space elevator after tether rupture," *J. Guid., Control, Dyn.*, vol. 36, no. 4, pp. 986–992, Jul. 2013, doi: 10.2514/1.59378.
[14] C. R. McInnes, "Dynamics of a particle moving along an orbital tower," *J. Guid., Control, Dyn.*, vol. 28, no. 2, pp. 380–382, Mar. 2005, doi: 10.2514/1.13505.
[15] S. S. Cohen and A. K. Misra, "The effect of climber transit on the space elevator dynamics," *Acta Astronautica*, vol. 64, nos. 5–6, pp. 538–553, Mar. 2009, doi: 10.1016/j.actaastro.2008.10.003.
[16] P. Williams and W. Ockels, "Climber motion optimization for the tethered space elevator," *Acta Astronautica*, vol. 66, nos. 9–10, pp. 1458–1467, May 2010, doi: 10.1016/j.actaastro.2009.11.003.
[17] Y. Ishikawa, K. Otsuka, Y. Yamagiwa, and H. Doi, "Effects of ascending and descending climbers on space elevator cable dynamics," *Acta Astronautica*, vol. 145, pp. 165–173, Apr. 2018, doi: 10.1016/j.actaastro.2018.01.031.
[18] P. Williams, "Dynamic multibody modeling for tethered space elevators," *Acta Astronautica*, vol. 65, nos. 3–4, pp. 399–422, Aug. 2009, doi: 10.1016/j.actaastro.2008.11.016.
[19] G. Shi, G. Li, Z. Zhu, and Z. H. Zhu, "Dynamics and operation optimization of partial space elevator with multiple climbers," *Adv. Space Res.*, vol. 63, no. 10, pp. 3213–3222, May 2019, doi: 10.1016/j.asr.2019.01.022.
[20] Z.-K. Wang, Y.-H. Fan, N.-G. Cui, and D. Liu, "Non-equatorial space elevator design approach," *Proc. Inst. Mech. Eng., G, J. Aerosp. Eng.*, vol. 233, no. 9, pp. 3235–3243, Jul. 2019, doi: 10.1177/0954410018797879.
[21] Z. Wang, N. Cui, Y. Fan, and D. Liu, "Modal and dynamic analysis of a tether for a nonequatorial space elevator," *IEEE Access*, vol. 6, pp. 74940–74952, 2018, doi: 10.1109/ACCESS.2018.2883363.
[22] A. A. Shabana, "Definition of the slopes and the finite element absolute nodal coordinate formulation," *Multibody Syst. Dyn.*, vol. 1, no. 3, pp. 339–348, Sep. 1997, doi: 10.1023/A:1009740800463.
[23] Z. H. Zhu, S. A. Meguid, and L. S. Ong, "Dynamic multiscale simulation of towed cable and body," in *Proc. Comp. Fluid Solid Mech.*, Cambridge, U.K., Jun. 2003, pp. 800–803.
[24] Z. H. Zhu, "Dynamic modeling of cable system using a new nodal position finite element method," *Int. J. Numer. Method. Biomed. Eng.*, vol. 26, no. 6, pp. 692–704, Jun. 2010, doi: 10.1002/cnm.1161.
[25] S. Luo, Y. Fan, and N. Cui, "Application of absolute nodal coordinate formulation in calculation of space elevator system," *Appl. Sci.*, vol. 11, no. 23, pp. 1–16, Dec. 2021, doi: 10.3390/app112311576.
[26] K. Otsuka and K. Makihara, "Absolute nodal coordinate beam element for modeling flexible and deployable aerospace structures," *AIAA J.*, vol. 57, no. 3, pp. 1343–1346, Mar. 2019, doi: 10.2514/1.J057780.
[27] S. Lu, X. Qi, Y. Hu, B. Li, and J. Zhang, "Deployment dynamics of large space antenna and supporting arms," *IEEE Access*, vol. 7, pp. 69922–69935, 2019, doi: 10.1109/ACCESS.2019.2918614.
[28] Z. Bai and X. Jiang, "Effects of orbital perturbations on deployment dynamics of tethered satellite system using variable-length element," *IEEE Access*, vol. 9, pp. 22399–22407, 2021, doi: 10.1109/ACCESS.2021.3056458.
[29] K. Otsuka, Y. Wang, K. Fujita, H. Nagai, and K. Makihara, "Multifidelity modeling of deployable wings: Multibody dynamic simulation and wind tunnel experiment," *AIAA J.*, vol. 57, no. 10, pp. 4300–4311, Oct. 2019, doi: 10.2514/1.J058676.
[30] X. Sun, M. Xu, and R. Zhong, "Dynamic analysis of the tether transportation system using absolute nodal coordinate formulation," *Acta Astronautica*, vol. 139, pp. 266–277, Oct. 2017, doi: 10.1016/j.actaastro.2017.07.020.
[31] F. J. Sun, Z. H. Zhu, and M. LaRosa, "Dynamic modeling of cable towed body using nodal position finite element method," *Ocean Eng.*, vol. 38, no. 4, pp. 529–540, Mar. 2011, doi: 10.1016/j.oceaneng.2010.11.016.
[32] G. Q. Li and Z. H. Zhu, "Long-term dynamic modeling of tethered spacecraft using nodal position finite element method and symplectic integration," *Celestial Mech. Dyn. Astron.*, vol. 123, no. 4, pp. 363–386, Aug. 2015, doi: 10.1007/s10569-015-9640-5.
[33] G. Li, G. Shi, and Z. H. Zhu, "Three-dimensional high-fidelity dynamic modeling of tether transportation system with multiple climbers," *J. Guid., Control, Dyn.*, vol. 42, no. 8, pp. 1797–1811, Aug. 2019, doi: 10.2514/1.G004118.
[34] J.-P. Salvetat, G. Briggs, J.-M. Bonard, R. Bacsa, A. Kulik, T. Stöckli, N. Burnham, and L. Forró, "Elastic and shear moduli of single-walled carbon nanotube ropes," *Phys. Rev. Lett.*, vol. 82, no. 5, pp. 944–947, Feb. 1999, doi: 10.1103/PhysRevLett.82.944.
[35] D. A. Walters, L. M. Ericson, M. J. Casavant, J. Liu, D. T. Colbert, K. A. Smith, and R. E. Smalley, "Elastic strain of freely suspended single-wall carbon nanotube ropes," *Appl. Phys. Lett.*, vol. 74, no. 25, pp. 3803–3805, Jun. 1999, doi: 10.1063/1.124185.
[36] M.-F. Yu, B. S. Files, S. Arepalli, and R. S. Ruoff, "Tensile loading of ropes of single wall carbon nanotubes and their mechanical properties," *Phys. Rev. Lett.*, vol. 84, no. 24, pp. 5552–5555, Jun. 2000, doi: 10.1103/PhysRevLett.84.5552.
[37] A. Takakura, K. Beppu, T. Nishihara, A. Fukui, T. Kozeki, T. Namazu, Y. Miyauchi, and K. Itami, "Strength of carbon nanotubes depends on their chemical structures," *Nature Commun.*, vol. 10, no. 1, p. 3040, Jul. 2019, doi: 10.1038/s41467-019-10959-7.
[38] Y. Ishikawa, "Obayashi Corporation's space elevator construction concept," *JBIS J. Br. Interplanet. Soc.*, vol. 69, nos. 6–7, pp. 227–239, Jun./Jul. 2016.
[39] K. Makihara and R. Takahashi, "Survivability evaluation of electrodynamic tethers considering dynamic fracture in space-debris impact," *J. Spacecraft Rockets*, vol. 53, no. 1, pp. 209–216, Jan. 2016, doi: 10.2514/1.A33328.
[40] K. Makihara and N. Matsumoto, "Survival probability of hollow cylindrical mesh tether under space-debris impact," *J. Spacecraft Rockets*, vol. 53, no. 3, pp. 520–527, May 2016, doi: 10.2514/1.A33379.
[41] K. Makihara and S. Kondo, "Structural evaluation for electrodynamic tape tethers against hypervelocity space debris impacts," *J. Spacecraft Rockets*, vol. 55, no. 2, pp. 462–472, Mar. 2018, doi: 10.2514/1.A34023.

RYO KUZUNO was born in Akita, Japan, in 1998. He received the bachelor's degree in mechanical engineering from Tohoku University, Miyagi, Japan, in 2021, where he is currently pursuing the master's degree with the Department of Aerospace Engineering. His research interests include multibody dynamics and flexible space-tether analysis.

SHUONAN DONG received the bachelor's degree from Beihua University, China, in 2018, and the master's degree from the Department of Aerospace Engineering, Tohoku University, Japan, in 2021. He is currently pursuing the Ph.D. degree with Tohoku University. His research interests include the formulation of multibody systems and the analysis of flexible aerospace structures.

TAIKI OKADA was born in Tokyo, Japan, in 1999. He is currently pursuing the bachelor's degree with the Department of Aerospace Engineering, Tohoku University, Japan, under the supervision of Prof. Makihara and Assistant Prof. Otsuka. His current research interests include the formulation of multibody systems, the dynamic analysis of flexible space structures, and the application of Kalman filtering problems.

KEISUKE OTSUKA received the bachelor's, master's, and Ph.D. degrees from the Department of Aerospace Engineering, Tohoku University, in 2014, 2016, and 2020, respectively. Since 2020, he has been working as an Assistant Professor at Tohoku University. In 2015, he studied aerodynamics at the KTH Royal Institute of Technology, Sweden. In 2019, he was engaged in flexible aircraft research with the Load Control and Aeroelastics Laboratory, Imperial College London, U.K., as a Visiting Research Student. His research interests include multibody dynamics and aeroelasticity.

KANJURO MAKIHARA received the bachelor's degree in aeronautics and astronautics from The University of Tokyo, in 1998, and the Ph.D. degree from the Graduate School, The University of Tokyo, in 2004. He is currently pursuing the Doctor of Engineering degree. Since 2004, he has been an Aerospace Project Research Associate at JAXA/ISAS and has devoted himself to energy-recycling vibration suppression for space structures. After working as a Visiting Researcher at the University of Cambridge, U.K. He has been working as an Associate Professor of aerospace engineering at Tohoku University, since 2011, and in 2019, he became a Professor at Tohoku University. His current research interests involve semi-active vibration suppression, self-powered energy-harvesting, dynamics of flexible structures, and issues pertaining to space debris.